# A non-stationary index-flood model for precipitation extremes in transient Regional Climate Model simulations

Martin Hanel,[1] T. Adri Buishand,[1] and Christopher A. T. Ferro[2]

[1] Royal Netherlands Meteorological Institute (KNMI), De Bilt, Netherlands

[2] School of Engineering, Computing and Mathematics, University of Exeter, Exeter, UK

## Abstract

The Generalized Extreme Value (GEV) distribution has often been used to describe the distribution of daily maximum precipitation in observed and climate model data. The model developed in this paper allows the GEV location parameter to vary over the region, while the dispersion coefficient (the ratio of the GEV scale and location parameters) and the GEV shape parameter are assumed to be constant over the region. This corresponds with the index-flood assumption in hydrology. It is further assumed that all three GEV parameters vary with time such that the relative change in a quantile of the distribution is constant over the region. This non-stationary model is fitted to the 1-day summer and 5-day winter precipitation maxima in the river Rhine basin in a simulation of the RACMO regional climate model for the period 1950–2099 and the results are compared with gridded observations. Except for an underestimation of the dispersion coefficient of the 5-day winter maxima by about 35% the GEV parameters obtained from the observations are reasonably well reproduced by RACMO. A positive trend in the dispersion coefficient is found in the summer season, which implies that the relative increase of a quantile increases with increasing return period. In the winter season there is a positive trend in the location parameter and a negative trend in the shape parameter. For large quantiles the latter counterbalances the effect of the increase of the location parameter. It is shown that the standard errors of the parameter estimates are significantly reduced in the regional approach compared to those of the estimated parameters from individual grid box values, especially for the summer maxima.

## 1. Introduction

Regional climate models (RCMs) nested inside a global climate model provide useful information about potential local climate change. Precipitation extremes in RCM simulations have been analyzed in different ways. One method is to consider the change in a large empirical quantile of the daily precipitation amounts (e.g., the 99th percentile) or the properties of the exceedances of such a quantile [e.g., *Durman et al*., 2001; *Christensen and Christensen*, 2004]. An alternative is to fit an extreme-value distribution to the largest daily precipitation amount in a season [e.g., *Frei et al*., 2006; *Beniston et al*., 2007; *Goubanova and Li*, 2007] or year [e.g., *Huntingford et al*., 2003; *Fowler et al.*, 2005; *Ekström et al*., 2005]. Maxima of multi-day precipitation amounts are treated similarly in several of these studies.

A problem with extreme precipitation is that the likelihood of detecting a systematic change at a single grid box is generally small due to the large year-to-year variability. *Frei and Schär* [2001] mention, for instance, that a frequency change by a factor of 1.5 in daily events with an average return period of 100 days can be detected with a probability of only 0.2 in a 100-year record, assuming a smoothly varying trend component and temporal independence of extreme events. The decrease of this probability with increasing event magnitude limits the detection of systematic changes in extreme events at a single grid box.

Spatial pooling has been used to detect meaningful changes in extremes. *Frei et al*. [2006] and *Goubanova and Li* [2007] averaged an estimated quantile of the extreme-

53 value distribution over large regions. *Kendon et al.* [2008] studied the effectiveness of
54 spatial pooling for the detection of changes in the 95th percentile of wet-day
55 precipitation. An alternative is to assume that the most uncertain parameters of the
56 extreme-value distribution are constant over some region. The estimates of these
57 parameters based on the pooled data across the region are then generally more precise
58 than those from the data of an individual grid box, leading to a reduction of the standard
59 errors of the estimated quantiles of the distribution. This approach has its origin in
60 hydrology where it is known as regional frequency analysis. Although biases will be
61 introduced when the homogeneity assumptions are not met, simulation studies [e.g.,
62 *Lettenmaier et al.*, 1987; *Hosking and Wallis*, 1997] show that even in regions with
63 moderate amounts of heterogeneity, a regional frequency analysis is more accurate than
64 the at-site analysis.
65
66 The most popular method of regional frequency analysis is the index-flood method.
67 *Fowler et al*. [2005] and *Ekström et al*. [2005] applied this method to the 1-, 2-, 5-, and
68 10-day annual maximum precipitation amounts across the UK in two RCM simulations.
69 Apart from a change in the distribution parameters between the control and future
70 climate, these parameters do not vary over time in their application.
71
72 The purpose of this paper is to introduce an index-flood model with time-varying
73 parameters as a tool to summarize changes of extreme precipitation in transient RCM
74 simulations. The model is applied to daily precipitation in the river Rhine basin in the
75 RACMO-ECHAM5 simulation. In this part of Europe, short-period convective storms

76 may cause local flooding in summer, whereas in winter multi-day episodes may have
77 adverse impacts over large areas. As in *Frei et al.* [2006], we analyze the 1-day
78 precipitation maxima in summer and the 5-day precipitation maxima in winter.
79
80 The index-flood model is described in section 2. Section 3 provides some information
81 about the river Rhine basin, the RACMO-ECHAM5 simulation, and the observational
82 data sets that were used for validation. The results for the summer maxima are presented
83 in section 4 and those for the winter maxima in section 5. Section 6 presents the
84 conclusions.
85

## 86 2. Regional modeling of non-stationary precipitation extremes

### 87 2.1. Index-flood model

88 The idea behind the index-flood method is that the variables within a homogeneous
89 region are identically distributed after scaling with a site-specific factor, the index flood.
90 The $T$-year quantile $Q_T(s)$ of the distribution of the variable $X(s)$ at any given site $s$, i.e.,
91 the value that is exceeded with probability $1/T$, can then be written as

92 $$Q_T(s) = \mu(s) q_T , \qquad (1)$$

93 where $\mu(s)$ is the index flood and $q_T$ is a regional, dimensionless quantile function, in this
94 context often called the growth curve. The mean or median of the distribution of $X(s)$ is
95 usually chosen as the index flood.
96
97 A consequence of the index-flood assumption is that the coefficient of variation of $X(s)$
98 should be constant over the region of interest. This property is useful for identifying

99 homogeneous regions. A number of authors have found that the coefficient of variation of
100 the observed annual maximum precipitation is relatively large in dry areas and small in
101 wet, mountainous regions [see *Brath et al.*, 2003]. Nevertheless, the spatial variation in
102 the coefficient of variation of precipitation maxima is generally much less than that in the
103 mean.
104
105 The index-flood method has been used with different probability models for the
106 distribution of $X(s)$. For seasonal and annual precipitation maxima the generalized
107 extreme value (GEV) distribution is popular. This is a three-parameter distribution that
108 combines the three possible types of extreme value distributions (i.e., Gumbel, Fréchet,
109 and reverse Weibull distributions). Its distribution function is given by

110
$$F(x) = \exp\left\{-\left[1+\kappa\left(\frac{x-\xi}{\alpha}\right)\right]^{-\frac{1}{\kappa}}\right\}, \qquad \kappa \neq 0,$$

111 (2)

112
$$F(x) = \exp\left\{-\exp\left[-\left(\frac{x-\xi}{\alpha}\right)\right]\right\}, \qquad \kappa = 0,$$

113 with $\xi$, $\alpha$, and $\kappa$ the location, scale, and shape parameters, respectively. The shape
114 parameter controls the behavior of the tails of the distribution – positive values imply a
115 heavy upper tail (Fréchet distribution).
116
117 Apart from support from extreme value theory [e.g., *Coles*, 2001], the GEV distribution
118 has often been found to describe the distribution of observed or simulated precipitation
119 maxima well. For annual precipitation maxima of various durations *Schaefer* [1990],

120 *Alila* [1999], and *Kyselý and Picek* [2007], using L-moment ratio diagrams, observed that
121 the GEV distribution is generally superior to other candidate distributions. In addition,
122 *Alila* [1999] and *Kyselý and Picek* [2007] found that a goodness of fit test based on the L-
123 kurtosis did not reject the GEV distribution. *Buonomo et al.* [2007] and *Goubanova and*
124 *Li* [2007] used the Kolmogorov-Smirnov goodness of fit test and concluded that the GEV
125 distribution is appropriate for modeling precipitation extremes in RCM projections for
126 most parts of Europe, although problems were met in dry areas where most of the
127 seasonal maxima were zero.
128
129 For the development of our non-stationary GEV model it is convenient to use the location
130 parameter as the index flood, i.e., $\mu(s) = \xi(s)$, rather than the mean or the median. If the
131 seasonal maximum $X(s)$ at site $s$ follows a GEV distribution with parameters $\xi(s)$, $\alpha(s)$,
132 and $\kappa$(s), then the scaled seasonal maximum $X(s)/\xi(s)$ has a GEV distribution with
133 location parameter 1, scale parameter $\gamma(s) = \alpha(s)/\xi(s)$, and shape parameter $\kappa(s)$. The
134 index-flood method applies if $\gamma(s)$ and $\kappa(s)$ do not vary over the region, i.e., $\gamma(s) = \gamma$ and
135 $\kappa(s) = \kappa$. The dispersion coefficient $\gamma$ is analogous to the coefficient of variation.
136
137 The $T$-year quantile of the scaled seasonal maximum $X(s)/\xi(s)$ follows from equation (2)
138 by setting $F(q_T) = 1–1/T$, $\xi = 1$, and $\alpha = \gamma$:

139
$$q_T = 1 - \frac{\gamma}{\kappa}\left\{1 - \left[-\log\left(1 - \frac{1}{T}\right)\right]^{-\kappa}\right\}, \qquad \kappa \neq 0,$$

140 (3)

141 $$q_T = 1 - \gamma \log\left[ -\log\left(1 - \frac{1}{T}\right)\right], \qquad \kappa = 0 .$$

142 Note that $q_T = 1$ and $Q_T(s) = \xi(s)$ when $T = 1/(1–1/e) = 1.58$ years, the return period
143 corresponding to the location parameter. The growth curve is determined by $\gamma$ and $\kappa$. This
144 is also the case if $X(s)$ is scaled by the mean [*Buishand*, 1991; *Sveinsson et al.*, 2001] or
145 the median [*Northrop*, 2004]. However, the index flood then depends on $\gamma$ and $\kappa$, which is
146 inconvenient in the case of temporal trends in these parameters.
147
148 **2.2. Non-stationary index-flood model**
149 A few studies in the hydrological literature deal with non-stationarity in regional
150 frequency analysis. *Cunderlik and Burn* [2003] assume temporal and spatial variation in
151 both the location and scale parameter of the distribution. Linear trends in these
152 parameters were estimated with a distribution-free method due to *Sen* [1968]. In a
153 subsequent paper [*Cunderlik and Ouarda*, 2006] the scale parameter was assumed to be
154 constant over the region of interest but still time-varying. The regional scale parameter
155 was estimated as a weighted average of the at-site scale parameters. *Renard et al.* [2006]
156 used a regional non-stationary GEV model to describe trends in annual maximum
157 discharges. In that model the shape parameter was constant but the scale and location
158 parameters varied over the region and there was a common linear trend in the location
159 parameter. Statistical inference was based on a Bayesian analysis using Markov chain
160 Monte Carlo methods. Other authors have successfully used a GEV distribution with
161 time-varying parameters, e.g., *Kharin and Zwiers* [2005], *Adlouni et al.* [2007], *García et*
162 *al.* [2007], and *Brown et al.* [2008], although not in the framework of regional frequency
163 analysis.

Let $X(s, t)$ be the seasonal maximum at site $s$ in year $t$. Using the location parameter of the GEV distribution as the index flood, the $T$-year quantile $Q_T(s, t)$ can be represented as

$$Q_T(s,t) = \xi(s,t) q_T(t), \quad (4)$$

where $q_T(t)$ is given by equation (3) but with time-dependent dispersion coefficient $\gamma(t)$ and shape parameter $\kappa(t)$. The location parameter $\xi(s, t)$ varies both in time and space. As in the non-stationary GEV model of *Renard et al.* [2006], the temporal trend in the location parameter is assumed to be constant over the region of interest. A motivation for this is that changes in extreme precipitation are mainly associated with large-scale changes in the atmospheric conditions (changes of the amount of precipitable water due to temperature change and changes of the atmospheric circulation). However, in regions with strong orography the changes in precipitation may be altitude-dependent [*Giorgi et al.*, 1997]. The altitude-dependence of the trend in the location parameter will be examined for the mountainous southern part of the Rhine basin.

We propose the following model for the GEV parameters:

$$\xi(s,t) = \xi_0(s) \exp[\xi_1 I(t)] \quad (5)$$

$$\gamma(t) = \exp[\gamma_0 + \gamma_1 I(t)] \quad (6)$$

$$\kappa(t) = \kappa_0 + \kappa_1 I(t) \quad (7)$$

where $I(t)$ is a time indicator or time-dependent covariate, the choice of which is discussed in section 3. Different forms of trends can be considered, but our choices have the following advantages. The dispersion coefficient cannot become negative because of the exponential expression in equation (6). The exponential function in equation (5)

ensures that the relative changes in the quantiles are constant over the region of interest, as follows. From equations (4) and (5), the relative change of the $T$-year quantile between years $t_1$ and $t_2$ at site $s$ can be written as

$$\frac{Q_T(s,t_2)}{Q_T(s,t_1)} = \frac{\xi(s,t_2)}{\xi(s,t_1)}\frac{q_T(t_2)}{q_T(t_1)} = \exp\{\xi_1[I(t_2)-I(t_1)]\}\frac{q_T(t_2)}{q_T(t_1)}, \qquad t_2 \geq t_1, \tag{8}$$

which does not depend on $s$. Apart from the common usage of percentages for changes in extreme precipitation, a reason to assume constant relative changes rather than absolute changes is that specific humidity and hence atmospheric moisture would increase roughly exponentially with temperature (about 6.5% per degree) according to the Clausius-Clapeyron relation [e.g., *Pall et al.*, 2007].

The parameters $\xi_0(s)$, $\xi_1$, $\gamma_0$, $\gamma_1$, $\kappa_0$, and $\kappa_1$ of the model were estimated by maximizing the log-likelihood

$$L = \sum_{s=1}^{S}\sum_{t=1}^{N} L_{s,t}\left(\xi_0(s), \xi_1, \gamma_0, \gamma_1, \kappa_0, \kappa_1\right) \tag{9}$$

where $L_{s,t}(\xi_0(s), \xi_1, \gamma_0, \gamma_1, \kappa_0, \kappa_1)$ is the log-likelihood for the seasonal maxima at grid box $s$ in year $t$, $S$ is the number of grid boxes in the region and $N$ is the number of years in the record. The number of parameters that has to be determined is thus $S$+5. Dealing usually with more than 50 grid boxes in one region it was difficult to estimate all parameters simultaneously. Therefore, a two-step procedure was applied [*Arnell and Gabriele*, 1988; *Buishand*, 1991]. Initial values of the parameters were based on L-moments estimates [*Hosking and Wallis*, 1997]. For the parameters $\xi_0(s)$ the individual grid box estimates were used, and the parameters $\gamma_0$ and $\kappa_0$ were set to the regional average of the grid-box

209 estimates. The trend parameters $\xi_1$, $\gamma_1$, and $\kappa_1$ were set initially to zero. In the first step, all
210 the site-specific location parameters $\xi_0(s)$ were estimated by maximum likelihood,
211 keeping the regional parameters $\xi_1$, $\gamma_0$, $\gamma_1$, $\kappa_0$, and $\kappa_1$ fixed. In the second step, the values
212 of $\xi_0(s)$ were fixed at their estimates from the previous step and the regional parameters
213 were estimated by maximum likelihood. These two steps were repeated until
214 convergence. The number of iterations needed for the procedure to converge was usually
215 not more than 5 for the summer and not more than 10 for the winter maxima. The CPU
216 time needed to fit the index-flood model was on average 10% larger in summer and 70%
217 larger in winter than the time needed to fit the model to each of the corresponding grid
218 boxes individually.
219
220 **2.3. Uncertainty and model checking**
221 The log-likelihood in equation (9) assumes independence between years and between
222 grid boxes within the region. In particular, the latter assumption is not satisfied because
223 the seasonal maxima at adjacent grid boxes are often associated with the same
224 meteorological event. As a consequence, the standard errors of the estimates can no
225 longer be obtained from the second derivatives of the log-likelihood. The bootstrap can
226 be used to assess the uncertainty of the parameters and quantiles of the distribution in the
227 case of spatial dependence. Rather than bootstrapping the data of the grid boxes
228 individually, the data for a certain year are bootstrapped simultaneously in order to
229 preserve the spatial dependence [cf. *Faulkner and Jones*, 1999; *Kharin et al.*, 2007].
230 Since resampling requires that the data come from the same distribution, the trend is
231 removed from the maxima $X(s, t)$ by the transformation [*Coles*, 2001]

$$\widetilde{X}(s,t) = \frac{1}{\hat{\kappa}(t)} \log\left[1 + \frac{\hat{\kappa}(t)}{\hat{\gamma}(t)}\left(\frac{X(s,t)}{\hat{\xi}(s,t)} - 1\right)\right], \tag{10}$$

where $\widetilde{X}(s,t)$ are the detrended seasonal maxima and $\hat{\xi}(s,t)$, $\hat{\gamma}(t)$, and $\hat{\kappa}(t)$ are the maximum likelihood estimates of the GEV parameters (these are obtained by replacing $\xi_0(s)$, $\xi_1$, $\gamma_0$, $\gamma_1$, $\kappa_0$, and $\kappa_1$ in equations (5)–(7) by their maximum likelihood estimates $\hat{\xi}_0(s), \hat{\xi}_1, \hat{\gamma}_0, \hat{\gamma}_1, \hat{\kappa}_0$, and $\hat{\kappa}_1$). Then a sample $t_1,\ldots,t_u,\ldots,t_N$ is drawn with replacement from the years $1,\ldots,N$. A bootstrap sample of detrended seasonal maxima is obtained by taking the vector $\left(\widetilde{X}(1,t_u),\ldots,\widetilde{X}(s,t_u),\ldots,\widetilde{X}(S,t_u)\right)$ for each resampled year $t_u$. Finally, the sample is transformed back to the original scale according to

$$X(s,u) = \hat{\xi}(s,u)\left\{1 + \hat{\gamma}(u)\frac{\exp[\hat{\kappa}(u)\widetilde{X}(s,t_u)] - 1}{\hat{\kappa}(u)}\right\} \tag{11}$$

and the parameters are re-estimated.

The transformed maxima $\widetilde{X}(s,t)$ should have a standard Gumbel distribution if the model is correct (we refer to them as standard Gumbel residuals hereafter), which is tested in this study by calculating the Anderson-Darling statistic for each grid box. The Anderson-Darling statistic $A^2$ is defined as [*Anderson and Darling*, 1952]

$$A^2 = N\int_{-\infty}^{\infty} \frac{[F_N(x) - F(x)]^2}{F(x)[1 - F(x)]}\, dF(x), \tag{12}$$

where $F_N(x)$ is the empirical distribution of the $\widetilde{X}(s,t)$ for the grid box of interest and $F(x)$ is the standard Gumbel distribution function, $F(x) = \exp[-\exp(-x)]$. The $A^2$ statistic summarizes the mean square distance between the two distributions, putting more weight on the tails of the distribution through the function $1/\{F(x)\,[1-F(x)]\}$. For testing

goodness of fit of extreme value distributions it has been shown [e.g., *Shimokawa and Liao*, 1999; *Laio*, 2004] that this statistic is more powerful than the Kolmogorov-Smirnov and Cramer-von Mises statistics and the probability plot correlation coefficient. Here $A^2$ also tests the adequacy of assumptions about the GEV parameters (the index-flood assumption, constant trends over the region of interest and (log-)linearity with the time indicator $I(t)$). Separate tests for these assumptions can be designed but these are not considered in the present paper. The definition of the region should be re-examined or a different model for the GEV parameters should be used if the fit is not acceptable.

The procedures used to assess uncertainty and goodness of fit assume independence between years. This assumption has been checked by exploring the temporal pattern of residuals. For this purpose, it is convenient to work with residuals that have a symmetric distribution, in particular the normal distribution. Standard normal residuals $\widetilde{X}_{\text{norm}}(s,t)$ are obtained by the transformation

$$\widetilde{X}_{\text{norm}}(s,t) = \Phi^{-1}\left\{\exp\left[-\exp\left(-\widetilde{X}(s,t)\right)\right]\right\}, \qquad (13)$$

with $\Phi^{-1}$ the quantile function of the standard normal distribution.

## 3. Rhine basin and data used

The river Rhine basin has an area of 185,000 km$^2$ and is situated in the territory of nine European countries (Figure 1a). The basin stretches from the Alps in the south with mountain peaks higher than 4000 m to a flat delta in the Netherlands in the north. Mean annual precipitation is quite variable – the wettest part is the Alpine region with more than 3000 mm of precipitation per year in some areas, the driest part is the area around

Mainz in the center of the Rhine basin where mean annual precipitation is about 400 mm. The overall mean annual precipitation is 910 mm.

The precipitation maxima in the output of the KNMI regional climate model RACMO [*van Meijgaard et al.*, 2008] driven by the ECHAM5 global climate model [*Jungclaus et al.*, 2006] under the SRES A1B emission scenario [*Nakićenović and Swart*, 2000] for the period 1950–2099 were studied. The horizontal resolution of the RACMO model is ≈ 25 km on a rotated longitude-latitude grid. There are 316 grid boxes whose centers lie within the Rhine basin (Figure 1b).

To use the index-flood model homogeneous regions have to be identified. *Hosking and Wallis* [1997] mention several methods for choosing the regions ranging from subjective partitioning to using geographical units and objective partitioning. The latter still requires subjective choices at several stages. We split the Rhine basin into regions subjectively: we estimated the GEV parameters at each grid box for the 1-day summer (JJA) and 5-day winter (DJF) maxima for two time slices (1950–1989 and 2070–2099) using the stationary model, i.e., with $I(t) = 0$ in equations (5)–(7). Since the grid box estimates of the shape parameter are not very reliable, we based the division of the Rhine basin on the spatial pattern of the dispersion coefficient. Spatial heterogeneity of the dispersion coefficient turned out to be stronger for the summer maxima (Figure 1b–c) than for the winter maxima and therefore has more influence on the delimitation of the regions. On the basis of Figure 1b–c we divided the Rhine basin into 5 regions (Figure 1d), each including 48 to 97 grid boxes. Region 1 corresponds roughly to the Swiss part of the

298 basin and region 5 to the Dutch part. The sensitivity of the results to the boundaries of the
299 regions was briefly checked by moving a few grid boxes from one region to another
300 region and refitting the model. There was little change in the estimated parameters and
301 the goodness of fit.
302
303 Figure 2 shows the change of the mean seasonal and annual precipitation between the
304 periods 1950–1989 and 2070–2099. In the model output mean annual precipitation
305 increases by about 5% over the whole basin, mean winter precipitation increases by more
306 than 20% over most of the basin and mean summer precipitation decreases by 10–20%.
307
308 The model for the GEV parameters defined in equations (5)–(7) requires the choice of the
309 time indicator $I(t)$. The most straightforward approach is to use $I(t) = t$. Since the
310 enhanced greenhouse effect is small during the first decades of the RCM simulation, a
311 more complicated function of the year $t$ is needed to allow the GEV parameters to stay
312 constant or almost constant in this period. Such a function usually contains one or more
313 unknown parameters which generally leads to more uncertain trend estimates. An
314 alternative time indicator which is representative of the enhanced greenhouse effect is the
315 global temperature. In our application a seasonal global temperature anomaly from the
316 driving ECHAM5 model is used. This anomaly is calculated with respect to the overall
317 1950–2099 mean temperature so that the parameters $\xi_0(s)$ are approximately orthogonal
318 to the regional parameters $\xi_1$, $\gamma_0$, $\gamma_1$, $\kappa_0$, and $\kappa_1$. This significantly speeds up the two-stage
319 estimation procedure. Using temperature anomalies with respect to some historical period
320 such as 1960–1989 (or temperature itself) leads to a significant correlation between

321 $\hat{\xi}_0(s)$ and $\hat{\xi}_1$. For example, if the historical period 1960–1989 is considered, the average
322 correlation between these parameters is –0.87. This correlation is only 0.14 if the
323 anomalies are calculated with respect to the overall mean. The summer and winter global
324 temperature anomaly is given in Figure 3. The increase between the periods 1950–1989
325 and 2070–2099 is ≈ 3 °C in the summer and ≈ 3.5 °C in the winter season in the
326 ECHAM5 simulation. The increase of the temperature over the Rhine basin is 3.3 °C in
327 summer and 2.8 °C in winter in the RACMO-ECHAM5 simulation. In the summer
328 season there is, however, a considerable gradient in the warming over the Rhine basin
329 (from 2.5 °C in region 5 in the north to 4.3 °C in region 1 in the south).
330
331 To compare the distribution of extremes in the RACMO-ECHAM5 run with that in
332 observations, the gridded observed daily precipitation amounts produced within the EU-
333 funded ENSEMBLES project [*Haylock et al.*, 2008] were used. These data (further
334 denoted as E-OBS) are available on different grids including a rotated longitude-latitude
335 grid with a resolution of ≈ 25 km, which makes the comparison with the RACMO data
336 straightforward. The data cover the period 1950–2006. The density of stations used for
337 gridding varies across the Rhine basin (e.g., Netherlands ≈ 1 station per 400 km$^2$,
338 Switzerland ≈ 1 station per 1300 km$^2$, and Germany ≈ 1 station per 3400 km$^2$). The rather
339 low station density in much of the Rhine basin implies that only a small fraction of grid
340 boxes contains one or more rainfall stations (see Figure 1d). For the gridding of the E-
341 OBS data set, the station data were first interpolated to a 0.1 degree longitude-latitude
342 grid (≈ 10 km by 5 km) using a search radius of 450 km, and then averaged within the
343 grid boxes. The distance between stations that significantly contribute to the interpolated

values is relatively large in areas with low station density, resulting in a large amount of spatial smoothing. This questions the representativeness of the extremes in the E-OBS data for these areas. *Hofstra et al*. [2009] compared daily precipitation in the E-OBS data to that in three gridded data sets based on a significantly larger number of rain gauges: one for the UK (1958–2002), the Alpine data set (1971–1995), and the ELDAS data set (October 1999–December 2000) covering central and northern Europe. The upper deciles of the area-average daily rainfall amounts found in these data sets turned out to be larger than those in the E-OBS data set, in particular in the Alpine data set. The latter is also used in our study and will be denoted as ALP from here on. It is available on a regular longitude-latitude grid with a resolution of ≈ 25 km. The density of stations used for gridding was ≈ 1 station per 100–200 $km^2$ and more high-elevation stations were included than in the E-OBS data. Further details on this data set can be found in *Frei and Schär* [1998].

## 4. Summer maxima

### 4.1. Results

Figure 4 shows boxplots of estimated parameters and their trends for the 1-day summer maximum precipitation. These boxplots were obtained from 3000 bootstrap samples. The upper panels (Figures 4a–c) refer to the GEV parameters for the period 1950–1989. The estimated values of $\overline{\xi}$ (average location parameter over the $S$ grid boxes in the region), $\gamma$, and $\kappa$ were derived from equations (5)–(7) using the 1950–1989 average summer global temperature anomaly for $I(t)$.

In the RACMO-ECHAM5 simulation the average location parameter is about 32 mm in the Alpine area and about 21 mm in the rest of the basin. This difference is caused by the high mean seasonal precipitation amounts in the Alps. The dispersion coefficient varies between 0.32 and 0.37 in the RACMO-ECHAM5 simulation. The high value of the dispersion coefficient in region 3 could be related to the low mean precipitation in this region. We do not have any explanation for the high values of the dispersion coefficient in region 5. The shape parameter is positive (Fréchet distribution).

Figures 4a–c also give the estimated parameters from the E-OBS and ALP data sets based on the non-stationary GEV model using the average summer global temperature anomaly from the HadCRUT3 data set of gridded observed temperatures [*Brohan et al.*, 2006] for $I(t)$ in equations (5)–(7). The location parameter in the RACMO-ECHAM5 simulation is on average 10% larger than the location parameter from the E-OBS data. In addition to model error, this difference is caused in part by the low number of stations used for gridding in certain countries (see section 3). This is most pronounced in region 1 where the average estimate of the location parameter from the E-OBS data is 20% lower than that from the ALP data which are based on a substantially larger number of stations. These differences remain large (15%) if the parameters for the E-OBS and ALP data are estimated for the common period 1971–1995. Furthermore, there is little difference between the estimated location parameter from the RACMO-ECHAM5 and E-OBS data in region 5 where the gridding of the E-OBS data was based on a relatively large number of stations. The dispersion coefficient and the shape parameter show a reasonable agreement in the E-OBS and ALP data sets for region 1. These two parameters are in

most regions somewhat larger in the RACMO-ECHAM5 simulation than in the E-OBS data.

Figures 4d–f refer to the estimated trends in the GEV parameters $\xi(t)$, $\gamma(t)$, and $\kappa(t)$. The change of $\xi(t)$ and $\gamma(t)$ is given as the ratio of the mean values of these parameters for the periods 2070–2099 and 1950–1989, the change of $\kappa(t)$ is the difference in the mean of $\kappa(t)$ for the same periods. There is a notable positive trend in the dispersion coefficient in all five regions, while the trends in the location and the shape parameters are less clear.

To assess the increase in precision of the parameter estimates due to spatial pooling, the non-stationary GEV model was fitted for each individual grid box (i.e., without spatial pooling) and the 25th and 75th percentiles of the parameter estimates were calculated using 500 bootstrap samples. Then, for each region and each parameter the average interquartile range was obtained as the difference between the average 75th and 25th percentile of the estimates. These average interquartile ranges were compared with those in Figure 4. Table 1 gives the reduction of the interquartile range for the summer season for the RACMO-ECHAM5 data. Note that in the case of no correlation between grid boxes the standard error would be roughly inversely proportional to the square root of the number of grid boxes, which would lead to a reduction by 85–90% of the interquartile range. If the grid boxes were perfectly dependent there would be no reduction at all. The reduction for the RACMO-ECHAM5 data is substantial: 30–80%. Spatial pooling has the largest influence on the uncertainty of the shape parameter and the reduction is larger for parameters describing trends.

413

414 The relative changes of quantiles (ratios of the average quantiles in the periods 2070–
415 2099 and 1950–1989) are shown in Figure 5. Despite the decrease of mean summer
416 precipitation, the quantiles of the extremes increase. The change of the 2-year quantile is
417 largely determined by the change of the location parameter. Therefore, there is only a
418 small increase (up to 10%) of the 2-year quantile except for region 2 where a relatively
419 large increase of the location parameter leads to an increase of this quantile of almost
420 30%. The relative increase of the 50-year quantile is larger in all regions except for
421 region 2 because of the positive trend in the dispersion coefficient. The 50-year quantile
422 increases by 10–30% in regions 1 and 3 and even by 50% in regions 4 and 5 where the
423 positive trend in the dispersion coefficient is enforced by the positive trend in the shape
424 parameter. The relatively small increase of the 50-year quantile in region 2 is caused by
425 the decrease of the shape parameter. The uncertainty of the change of a given quantile is
426 large, in general comparable with its magnitude.

427

428 One possible way to reduce the uncertainty of changes of quantiles is to join regions or to
429 assume that certain regions have common parameters. To test for differences between
430 regions the following statistic was used:

431 $$R = \sum_{i=1}^{n} (\hat{\theta}_i - \bar{\theta})^2 \qquad (14)$$

432 with $n$ the number of regions, $\hat{\theta}_i$ the estimate of the parameter of interest for region $i$ and
433 $\bar{\theta} = \sum_{i=1}^{n} \hat{\theta}_i / n$. The results of the test for the five regions in the Rhine basin are given in
434 Table 2. The $p$-values were obtained using a bootstrap procedure as described in

435 Appendix A. The differences between the regions are significant at the 0.1 level for all
436 parameters except the trend parameter $\gamma_1$. The differences in the trend parameters $\xi_1$ and
437 $\kappa_1$, however, are mostly due to the results in region 2 only: the trends in the other regions
438 are similar (see Figure 4). Therefore, a restricted model with common trends of the GEV
439 parameters in regions 1, 3, 4, and 5 was also fitted. Regardless of different values of
440 $\hat{\gamma}_0$ and $\hat{\kappa}_0$, the estimated changes of the quantiles for this restricted model are almost
441 identical in these four regions (see Figure 6) and roughly correspond to the mean of the
442 relative changes in these regions assuming no common parameters. The uncertainty is,
443 however, significantly reduced. For the 50-year quantile in Figure 6 a 27% increase is
444 found. This corresponds to a 6.3% increase per degree of summer warming in region 1
445 and a 10.8% increase per degree in region 5. The latter value is considerably larger than
446 that expected from the Clausius-Clapeyron relation, indicating that other factors than the
447 temperature influence on atmospheric moisture also determine the change in extreme
448 precipitation.
449
450 We studied the data further to find an explanation for the deviating trends in the location
451 parameter and the shape parameter for region 2. This region appeared to be part of a
452 larger area east of the Rhine basin exhibiting less summer drying than the rest of the
453 basin in the RACMO-ECHAM5 simulation (not shown). This difference in summer
454 drying might explain why the location parameter increases in region 2 and not in the
455 other regions. The increased soil moisture deficits towards the end of the 21st century
456 limit the increase of summer showers in regions 1, 3, 4, and 5. We further found that the
457 largest values in the last 20–30 years of the simulation for region 2 are not as large as in

458 the rest of the simulation: the trend is different there. This might explain the drop in the
459 shape parameter in this region (Figure 4f).
460
461 Seven alternative temperature anomalies were considered to explore the sensitivity of the
462 changes in the GEV parameters and quantiles to the time indicator $I(t)$. Smoothed
463 summer global temperature anomalies using a locally weighted regression, "loess"
464 [*Cleveland*, 1979] as well as smoothed and non-smoothed annual global temperature
465 anomalies were obtained from the driving ECHAM5 model. Smoothed summer and
466 annual temperature anomalies of the whole RACMO domain as well as of the Rhine
467 basin were calculated using the RACMO data. The values of the trend parameters $\xi_1$, $\gamma_1$
468 and $\kappa_1$ depend on the range of the temperature anomalies: the larger the range the lower
469 the values of these parameters. Table 3 gives the average changes in the GEV parameters
470 and quantiles over regions 1, 3, 4, and 5. These changes are almost the same for the
471 various choices of the time indicator $I(t)$.
472
473 **4.2. Model validation**
474 For the RACMO-ECHAM5 simulation, the goodness of fit was tested using the $A^2$
475 statistic. For regions 1 and 3, Figure 7 gives the $A^2$ value for each grid box together with
476 critical values for a test at the 0.1 significance level. These critical values were
477 determined using a parametric bootstrap procedure (Appendices B and C). The local 0.1
478 critical values in Figure 7 apply to the goodness of fit test at an individual grid box. The
479 likelihood that all $A^2$ values fall below these critical values is small. In the case of an
480 adequate fit it is expected that 10% of the $A^2$ values exceed the local 0.1 critical value.

481 This fraction is higher for regions 1 and 3 (≈ 20%). This does not necessarily imply lack
482 of fit because of spatial dependence. Even if the model provides an adequate fit, clusters
483 of grid boxes may fail the Anderson-Darling test in the case of spatial dependence. In
484 order to evaluate the field significance, the 0.1 global critical values in Figure 7 have to
485 be considered. The chance that some $A^2$ value exceeds the line of these critical values is
486 0.1 if the data come from the assumed model. None of the $A^2$ values for region 1 is above
487 this line, but in region 3 there are five grid boxes for which $A^2$ exceeds the global 0.1
488 critical value. Four of these grid boxes are situated near Mainz in the center of the region
489 (Figure 1) where the lowest precipitation in the Rhine basin is found. A separate model fit
490 for these four grid boxes and three adjacent grid boxes with large $A^2$ values revealed a
491 relatively high dispersion coefficient for this subregion. There was no evidence of lack of
492 fit of the GEV distribution and the trend $\gamma_1$ in the dispersion coefficient did not deviate
493 much from that for the rest of region 3. These seven grid boxes in this relatively dry area
494 were excluded. In addition, four grid boxes in region 4 for which $A^2$ exceeds the global
495 0.1 critical value were excluded too. One of these grid boxes is located on the western
496 border of the river Rhine basin, whereas the other three are situated in a relatively wet
497 subregion, known as Sauerland, with grid box estimates of $\gamma_0$ lower than those for the rest
498 of this region. The GEV model was then fitted again and the $A^2$ statistics and their critical
499 values were recalculated. The results discussed in section 4.1 refer to the refitted model
500 as well as Figures 4, 5, and 6. Figure 8 shows the location of the excluded grid boxes and
501 summarizes the results of the goodness of fit tests. In region 3 there remains one grid box
502 for which $A^2$ exceeds the global 0.1 critical value.
503

Two additional checks were made to assess the presence of temporal dependence: (1) the standard normal residuals were averaged over each of the five regions and smoothed using "loess", in order to find significant temporal patterns; (2) the average autocorrelation of the standard normal residuals was calculated for each of the five regions. Figures 9 and 10 show the results of these checks for region 1. Both pictures are representative of the other regions as well and both show no evidence of temporal dependence.

# 5. Winter maxima

## 5.1. Results

Boxplots of the estimated GEV parameters for the 5-day winter maximum precipitation in the RACMO-ECHAM5 simulation for the period 1950–1989 are given in Figures 11a–c. As for the summer season the location parameter in the Alpine region is higher than in the rest of the basin. The dispersion coefficient shows a south north gradient. The shape parameter is almost zero in three of the five regions.

The RACMO-ECHAM5 simulation overestimates the location parameter by 10–30% and underestimates the dispersion coefficient by 35% with respect to the E-OBS data.
For the 5-day winter maxima the reduction of variability in the E-OBS data due to the gridding of insufficient station data is smaller than for the 1-day summer maxima because of the stronger spatial correlation between the 5-day winter maxima. The low number of stations used for gridding cannot explain the observed differences between the parameter estimates from the RACMO-ECHAM5 and E-OBS data. In contrast to the 1-day summer

maxima the differences between the estimated location parameters from the ALP and E-OBS data are small for region 1. There is also a significant difference between the estimated location parameters from the RACMO-ECHAM5 and E-OBS data for the well-gauged region 5. The overestimation of the location parameter in the RACMO-ECHAM5 data is strongly related to the positive model bias in the mean (36%) and the standard deviation (11%) of daily winter precipitation. Part of this bias is caused by the systematic undercatch inherent to rain gauges for which neither the E-OBS nor the ALP data were corrected. For instance, *Frei et al.* [2003] mention for the winter season an average bias of 11% due to undercatch. This bias is expected to be somewhat lower in other parts of the Rhine basin because of a smaller fraction of snowfall. Since the overestimation of the standard deviation is smaller than that of the mean, the coefficient of variation is underestimated (19%). The low relative variability of the daily values in the RACMO-ECHAM5 simulation partly accounts for the underestimation of the dispersion coefficient in the GEV model for the 5-day maxima across the basin.

The estimated trends of the GEV parameters in the RACMO-ECHAM5 simulation are shown in Figures 11d–f. The location parameter increases and the shape parameter decreases significantly over the whole basin, while there is almost no change in the dispersion coefficient. The relative changes of the quantiles are given in Figure 12. Due to the increase of the location parameter the 2-year quantiles increase over the whole basin by 10–20%. The relative increase of these quantiles is, however, smaller than the relative increase of mean winter precipitation (Figure 2). For the 50-year quantiles the effect of the increase of the location parameter is counterbalanced by the decrease of the

550 shape parameter resulting in only a slight and non-significant change of this quantile. The
551 physical causes of the relatively small change at large quantiles are unknown and need
552 further investigation. The 5-day winter precipitation extremes result from intense large-
553 scale events which are strongly influenced by the atmospheric circulation. A detailed
554 study of the changes in circulation characteristics would therefore be of interest.
555
556 In the model fitted to the E-OBS data there is a rather strong positive trend in the location
557 parameter for all five regions (not shown). This trend is in line with the strong increase
558 found by *Hundecha and Bárdossy* [2005] in the 5-day winter maximum precipitation
559 during the period 1958–2001 at rainfall stations in the German part of the Rhine basin.
560 This upward trend is much stronger than that in the RACMO-ECHAM5 simulation.
561 Moreover, the Gumbel residuals for regions 2, 3, and 4 show a small, but statistically
562 significant lag 1 autocorrelation for the E-OBS data. This points to some unknown factor
563 (or factors) causing long-term variability in extreme 5-day winter precipitation.
564 *Hundecha and Bárdossy* [2005] did not find a significant increase in the frequency of
565 circulation patterns associated with wet days over their study period. The presence of this
566 long-term variability makes difficult the interpretation of the differences between the
567 estimated GEV parameters in the RACMO-ECHAM5 simulation and the E-OBS data set.
568 Further investigation is required to understand fully the disparities.
569
570 For the 5-day winter precipitation maxima in the RACMO-ECHAM5 data the reduction
571 of the interquartile ranges of parameter estimates due to spatial pooling is 17–53%, where
572 the lower limit applies to the parameter $\xi_1$ and the upper limit to the parameter $\kappa_1$. This

573 reduction is lower than that for the 1-day summer maxima, due to the stronger spatial
574 correlation between the 5-day winter precipitation maxima. In contrast to the summer
575 maxima, the test for differences between regions indicates that for the 5-day winter
576 precipitation maxima the trends in the GEV parameters can be assumed the same for the
577 whole Rhine basin. However, the reduction of the uncertainty of the quantiles by fitting a
578 model with common trend parameters $\xi_1$, $\gamma_1$, and $\kappa_1$ is not as large as that for the 1-day
579 summer maxima. This is partly due to the larger correlation between the estimated
580 parameters of different regions in winter and partly due to the fact that the uncertainty of
581 the changes in quantiles is smaller in winter (compare the widths of the confidence bands
582 in Figures 5 and 12).
583
584 Analogously to the summer season, the sensitivity of the changes in the GEV parameters
585 and quantiles to the time indicator $I(t)$ was explored using seven alternative winter and
586 annual temperature anomalies. The resulting changes (not shown) do not differ
587 significantly for these alternative choices.
588
589 **5.2. Model validation**
590 For the RACMO-ECHAM5 simulation, Figure 13 gives a summary of the goodness of fit
591 testing for the winter season. As for the summer season the model was initially fitted to
592 all grid boxes. Fifteen grid boxes with high values of $A^2$ were excluded. Most of these
593 grid boxes are located on the border of region 1 or close to it, some of them at high
594 altitude. Two excluded grid boxes are found on the border of region 4. After the
595 exclusion of these grid boxes the model was refitted and the $A^2$ values were recalculated.

596 The results discussed in section 5.1 refer to this refitted model. After refitting there
597 remains one grid box with an $A^2$ value exceeding the global 0.1 critical value in region 2.
598 In contrast to the observed data, no signs of persistence or low-frequency variability were
599 found in the standard normal residuals of the RACMO-ECHAM5 data (not shown). This
600 points to a failure of the driving ECHAM5 global model to reproduce long-term
601 variability. There is, however, a strong indication that the magnitude of the trend
602 parameter $\xi_1$ decreases with increasing altitude in the Swiss part of the Rhine basin (see
603 Figure 14). The relative increase in the GEV location parameter is therefore smaller at
604 high altitude. This is also found for the change in mean winter precipitation in the
605 RACMO-ECHAM5 simulation. Though the relative increase in mean winter precipitation
606 is smaller at high altitude, the absolute increase is larger. The latter is in agreement with
607 the RCM simulation of *Giorgi et al.* [1997]. The physical cause of this altitude-
608 dependence is not clear.
609

## 610 6. Conclusions

611 In the present study a non-stationary regional GEV model was introduced and applied to
612 the 1-day summer and 5-day winter precipitation maxima in the transient RACMO-
613 ECHAM5 run for the river Rhine basin in order to evaluate the changes in the properties
614 of simulated precipitation extremes. The capability of the climate model to reproduce
615 observed precipitation extremes was also assessed. The river Rhine basin was subdivided
616 into 5 regions and the GEV model was applied to each of these regions. The model
617 allows the location parameter to vary over the region of interest with common trend in

618 time. The dispersion coefficient and the shape parameter are assumed constant over the
619 region but varying with time.
620
621 The regional GEV model provides an informative summary of the differences between
622 observed and simulated precipitation maxima as well as of the changes in the distribution
623 of extremes. Looking at the parameters of the GEV distribution gives a better insight into
624 the differences in distribution than looking at a single quantile only. In addition, the
625 standard errors of the estimated common parameters are significantly reduced compared
626 to the estimates based on the data of an individual grid box.
627
628 The choice of regions is a difficult point in the application of the regional GEV model.
629 The size of a region is limited by spatial heterogeneities in the GEV parameters $\gamma$ and $\kappa$ as
630 well as spatial heterogeneities in the trends of these parameters. Maps of grid box
631 estimates of $\gamma$ for the periods 1950–1989 and 2070–2099 proved to be useful for the
632 partitioning of the Rhine basin in this study. Instead of defining certain regions, one could
633 pool the data from the grid box of interest and a fixed number of neighboring grid boxes
634 [e.g., *Zwiers and Kharin*, 1998; *Coelho et al*., 2008]. This is convenient if identifying
635 large, homogeneous regions is difficult or if one wishes to show how the model
636 parameters vary over the entire RCM domain. The size of such neighborhoods is
637 typically much smaller than the regions used in regional frequency analyses, and
638 therefore results in less spatial pooling. Moreover, the use of a fixed number of grid
639 boxes will not be optimal if the degree of spatial heterogeneity varies over the domain.
640

641 The values of estimated parameters in the period 1950–1989 for the 1-day summer
642 precipitation extremes are reasonably well reproduced in the RACMO-ECHAM5
643 simulation. Part of the differences between the values from the E-OBS data can be
644 ascribed to the low density of stations used for gridding. The distribution of the 5-day
645 winter precipitation extremes is affected by strong positive biases in the mean and
646 standard deviation of daily winter precipitation. In particular, the dispersion coefficient of
647 the GEV distribution is severely underestimated across the whole Rhine basin.
648
649 The changes of the distribution of the 1-day summer precipitation maxima are primarily
650 related to the positive trend in the dispersion coefficient. Since there is almost no change
651 in the location parameter, the changes in distribution are mainly found at large quantiles
652 (e.g., the 50-year quantile) whereas there are only minor changes in quantiles close to the
653 median (i.e., the 2-year quantile). For the 5-day winter maxima the low quantiles (e.g., 2-
654 year quantile) are increasing due to the increase of the location parameter. As the return
655 period gets longer the effect of the positive trend in the location parameter is
656 counterbalanced by the decrease of the shape parameter resulting in only minor positive
657 or negative changes of large quantiles (e.g., the 50-year quantile).
658
659 The opposite direction of the changes in mean and 1-day maximum precipitation in
660 summer is in agreement with earlier findings of *Christensen and Christensen* [2004] and
661 *Frei et al.* [2006]. A relatively small change of the quantiles of extreme multi-day winter
662 precipitation was also found by *Leander et al.* [2008] for the adjacent Meuse basin in a
663 simulation of the RACMO model driven by the HadAM3H atmospheric model of the

664 Hadley Centre. Despite a considerable increase in mean winter precipitation in this
665 experiment there was little change in the distribution of the 10-day winter precipitation
666 maxima and extreme river flows. The differences between changes in mean and extremes
667 indicate that proportional adjustment of observed data can be very misleading.
668
669 Despite the reduction of standard errors due to spatial pooling of data, the changes in the
670 quantiles of the extreme-value distributions are often not statistically significant. For the
671 2-year quantile of the 1-day summer maxima this can be attributed to the fact that the
672 change in the location parameter is small. The estimates of the relative changes of the 50-
673 year quantiles are strongly affected by the estimates of the dispersion coefficient and the
674 shape parameter, which have large standard errors. For the summer season the
675 uncertainty of the change in this quantile for regions 1, 3, 4, and 5 could be reduced
676 considerably by assuming common trend parameters $\xi_1$, $\gamma_1$, and $\kappa_1$. The use of an
677 ensemble of RACMO simulations driven by different simulations of the ECHAM5 global
678 climate model is an option to improve the estimates of the changes in extreme value
679 properties of this RCM-GCM configuration further. Apart from the uncertainty in the
680 extreme value properties for a particular RCM-GCM configuration, there are large
681 differences between the estimated changes for different RCM-GCM combinations.
682
683 The Anderson-Darling test shows that the model fits well for much of the Rhine basin. In
684 the summer the model fails to fit in a relatively dry subregion with a relatively high
685 dispersion coefficient and in a small relatively wet subregion. In the winter season the
686 model did not fit well at a number of grid boxes on, or close to, the border of the Rhine

687 basin, in particular in the Swiss part of the basin. As a consequence, a small number of
688 grid boxes were excluded. A separate model fit using part of the excluded grid boxes
689 suggests that formation of different, smaller regions could improve the goodness of fit,
690 however, at the cost of increased uncertainty. Another possibility is the reformulation of
691 the statistical model to allow the dispersion coefficient to vary over the region of interest.
692 In addition, for regions with strong orography it may be necessary to incorporate altitude-
693 dependence of the trend in the location parameter.
694

695 ## Appendix A: Test for differences between regions

696 Let $\theta_i$ be one of the parameters $\xi_1$, $\gamma_0$, $\gamma_1$, $\kappa_0$, or $\kappa_1$ in the non-stationary GEV model for
697 region $i$ and let $\boldsymbol{\tau}$ be the vector of the other parameters. We want to test the hypothesis
698 $\mathrm{H}_0 : \theta_1 = \theta_2 = \ldots = \theta_n$ using the statistic $R$ in equation (14). The test consists of the
699 following steps:
700

701 1. Calculate the value of the test statistic using equation (14) and denote this value $r$.
702 2. Calculate the standard Gumbel residuals using the $\hat{\theta}_i$ and the estimated values of the
703 other parameters.
704 3. Re-estimate the other parameters $\hat{\boldsymbol{\tau}}_0$ given $\theta_1 = \theta_2 = \ldots = \theta_n = \bar{\theta}$.
705 4. Draw a bootstrap sample from the standard Gumbel residuals using resampling of
706 years to preserve the spatial dependence structure (see section 2.3) and transform this
707 sample back to the original scale using the parameter estimates $\bar{\theta}$ and $\hat{\boldsymbol{\tau}}_0$.
708 5. Re-estimate all parameters and re-calculate the test statistic as

$$r_b^* = \sum_{i=1}^{n} (\hat{\theta}_{b,i}^* - \bar{\theta}_b^*)^2 \,, \qquad \text{(A1)}$$

with $\hat{\theta}_{b,i}^*$ the estimate of $\theta_i$ from bootstrap sample $b$ and $\bar{\theta}_b^* = \sum_{i=1}^{n} \hat{\theta}_{b,i}^* / n$.

6. Repeat steps 4–5 until the desired number of bootstrap samples is obtained.

The $p$-value is the fraction of $r_b^*$ values larger than $r$. The $p$-values in Table 2 are based on 500 bootstrap samples.

## Appendix B: Determination of the critical values of the Anderson-Darling statistic

The critical values of the Anderson-Darling statistic $A^2$ in the literature usually refer to the situation of independent realizations from a distribution that is entirely specified under the null hypothesis. This does not apply to the standard Gumbel residuals $\tilde{X}(s,t)$ at a given grid box, which are in fact dependent due to the use of estimated GEV parameters instead of their true but unknown values. It is well-known that parameter estimation has a substantial effect on the distribution of $A^2$ [e.g., *Laio*, 2004]. This appendix deals with the derivation of the local and global critical values of $A^2$ from bootstrap samples. The generation of these bootstrap samples is discussed in Appendix C. In our application $B$ = 3000 bootstrap samples were generated.

Let $t(s)$ be the value of $A^2$ from the climate model data at grid box $s$ ($s$ = 1, …, $S$) and let $t_b^*(s)$ be the value of $A^2$ from bootstrap sample $b$ ($b$ = 1, …, $B$ ) for this grid box. For a

chosen significance level $\alpha_{LOC}$, the local critical values $c^{\alpha_{LOC}}(s)$ are obtained for each grid box as the *k*th smallest value $t^*_{(k)}(s)$ of the $t^*_b(s)$, where $k = (1-\alpha_{LOC})(B+1)$.

The determination of the global critical values is based on an approach suggested by *Davison and Hinkley* [1997]. Let $c^{\alpha_{LOC}}_{-b}(s)$ be the local critical values that we get if we exclude bootstrap sample *b*. Then a bootstrap estimate of the global error rate $\alpha_{GLOB}$ is obtained as:

$$\alpha_{GLOB} = \frac{\#\{b : [t^*_b(s) \geq c^{\alpha_{LOC}}_{-b}(s), \quad \text{for any } s]\}}{B}, \tag{B1}$$

where $\#\{b: A_b\}$ is the number of *b* for which $A_b$ is true. This error rate can easily be calculated using the fact that bootstrap sample *b* fulfills the condition $[t^*_b(s) \geq c^{\alpha_{LOC}}_{-b}(s), \quad \text{for any } s]$ if and only if $\text{rank}[t^*_b(s)] \geq k = (1-\alpha_{LOC})(B+1)$ for at least one *s*. Thus if the values of $t^*_b(s)$ are stored in a matrix with grid boxes in columns and bootstrap samples in rows, then we first calculate the columnwise ranks and subsequently the proportion of rows in which the maximum rank is greater than or equal to *k.* The value of *k* is chosen such that $\alpha_{GLOB}$ is as close as possible to the desired global significance level.

## Appendix C: Comparison of two bootstrap procedures for goodness of fit testing

The determination of the critical values of the Anderson-Darling statistic $A^2$ requires simulation from the model under the null hypothesis. In particular, the preservation of

751 spatial dependence is important. The bootstrap procedure outlined in section 2.3 to asses
752 the uncertainty of the parameter estimates and quantiles is not appropriate for testing
753 goodness of fit because the distribution of the $\widetilde{X}(s,t)$ may deviate from the Gumbel
754 distribution due to lack of fit of the GEV model and because of the occurrence of ties in
755 the bootstrap samples. The latter influences the statistical properties of the empirical
756 distribution function $F_N(x)$ in equation (12). In this appendix two alternatives are
757 discussed:
758
759 • Replacement of resampled standard Gumbel residuals by samples from the
760 standard Gumbel distribution, preserving the spatial structure of the ranks of the
761 maxima as suggested by *Heffernan and Tawn* [2004]. This approach requires no
762 assumptions about the underlying dependence structure of data.
763
764 • Sampling standard normal residuals from the multivariate normal distribution
765 [*Hosking and Wallis*, 1997]. These residuals are assumed to be equicorrelated,
766 i.e., the correlation $\rho_{i,j}$ between the residual at grid box $i$ and the residual at grid
767 box $j$ equals $\rho_{i,j} = \rho$ for $i \neq j$ and $\rho_{i,j} = 1$ for $i = j$. In this case the multivariate
768 normal dependence structure is introduced into the simulated samples.
769
770 In the following the procedures are referred to as "HT" and "MVN", respectively, and
771 both are fully described below.
772
773 **Bootstrap procedure based on the Heffernan and Tawn approach**

1. Fit the statistical model to the original sample.
2. Calculate standard Gumbel residuals with the parameter estimates from step 1.
3. Bootstrap the residuals from step 2 (using resampling of years to preserve the spatial dependence as described in section 2.3).
4. Generate $S$ independent samples of size $N$ from the standard Gumbel distribution ($S$ is the number of grid boxes and $N$ the number of years).
5. Rearrange the values in the samples from step 4 such that the dependence structure of the ranks corresponds to that of the bootstrapped residuals from step 3.
6. Transform the rearranged standard Gumbel values from step 5 back to the original scale using the parameter estimates from step 1.
7. Fit the statistical model again.
8. Calculate standard Gumbel residuals with the parameter estimates from step 7 and calculate the $A^2$ statistics.
9. Repeat steps 3–8 until the desired number of bootstrap samples is obtained.

**Parametric bootstrap procedure with sampling from the multivariate normal distribution**

1. Fit the statistical model to the original sample.
2. Calculate standard normal residuals (see section 2.3) with the parameter estimates from step 1.
3. Calculate the average correlation $\hat{\rho}$ of the standard normal residuals.
4. Generate a sample of $S$ equicorrelated standard normal variables with correlation $\hat{\rho}$.

5. Transform the sample from step 4 back to the original scale using the parameter estimates from step 1.
6. Fit the statistical model again.
7. Calculate standard Gumbel residuals with the parameter estimates from step 6 and calculate the $A^2$ statistics.
8. Repeat steps 4–7 until the desired number of bootstrap samples is obtained.

A simulation experiment was conducted to assess the validity of both approaches: 3000 samples of size 150 from an equicorrelated 30-dimensional normal distribution with known correlation were generated (think about 30 grid boxes in the RACMO-ECHAM5 simulation which has a length of 150 years). These samples (further denoted as control samples) were transformed according to the non-stationary GEV model

$$\xi(s,t) = \xi_0(s)\exp[\xi_1(t-40)_+] \quad \text{(C1)}$$

$$\gamma(t) = \exp[\gamma_0 + \gamma_1(t-40)_+] \quad \text{(C2)}$$

$$\kappa(t) = \kappa_0 + \kappa_1(t-40)_+ \quad \text{(C3)}$$

with $s = 1, \ldots, 30$; $t = 1, \ldots, 150$, and $(x)_+ = \max(x, 0)$. The values of the parameters were set to be representative of those obtained for the 1-day summer maximum precipitation in the Rhine basin, i.e., $\xi_0(s)$ ranged between 22 and 38, $\xi_1 = 0.00055$, $\exp(\gamma_0) = 0.37$, $\gamma_1 = 0.0013$, $\kappa_0 = 0.05$, and $\kappa_1 = 0.00015$.

For each sample the parameters of the GEV model were estimated and the values of the $A^2$ statistics were calculated. The 0.1 critical value from these simulations is denoted the "true" critical value. Further, for one of the control samples two sets of 3000 bootstrap

819 samples were generated using the "HT" and "MVN" approaches, respectively, and the 0.1
820 local and global critical values of the $A^2$ statistic were calculated according to Appendix
821 B.
822
823 Table C1 gives the local rejection rates of the null hypothesis as obtained from the
824 control samples, i.e., the proportion of the $A^2$ values of these samples lying above the
825 "HT" and "MVN" critical values. For the "MVN" critical values the rejection rate
826 corresponds quite well with the nominal 0.1 significance level, but for the "HT" critical
827 values the actual rejection rate is lower than 0.1 in the case of correlation and the
828 difference grows with increasing correlation coefficient. Table C1 further shows that the
829 "MVN" critical values resemble the "true" critical values and decrease with increasing
830 correlation. By contrast the "HT" critical values do not depend on correlation. Though
831 Table C1 refers to the local rejection rates and the local critical values, very similar
832 results were obtained for the global test at the 0.1 significance level.
833
834 To understand why the critical values of the $A^2$ statistic are decreasing with increasing
835 correlation, we have to examine how the estimates of the parameters are influenced by
836 the data from a particular grid box. The estimate of $\xi_0(s)$ is largely determined by the
837 maxima of the grid box of interest. If there is no or little correlation, the maxima of this
838 grid box have little influence on the estimates of the other parameters $\gamma_0$, $\kappa_0$, $\xi_1$, $\gamma_1$, and $\kappa_1$.
839 The influence of the maxima of the grid box of interest on the estimates of these
840 parameters grows with increasing spatial correlation. As a result the fitted regional GEV
841 model will describe the local maxima better and therefore the critical value of the $A^2$

842 statistic should be smaller than in the case of independence. The "MVN" and "true"
843 critical values for $\rho = 0.99$ are close to the critical value for the case that all six
844 parameters are estimated from the maxima at the grid box of interest only.
845
846 The reason of the failure of the "HT" approach in the case of goodness of fit testing is
847 that the test statistic is insensitive to a permutation of the data, i.e., rearranging residuals
848 at a grid box to preserve the spatial dependence of the ranks does not influence the value
849 of the $A^2$ statistic. Unlike the "MVN" bootstrap samples, the values of the $A^2$ statistic do
850 not exhibit any spatial correlation in the "HT" bootstrap samples. Although the "HT"
851 approach is not suitable for goodness of fit testing, it can be used for the estimation of
852 standard errors and the construction of confidence intervals, for which it was originally
853 introduced by *Heffernan and Tawn* [2004].
854
855 It is not surprising that the "MVN" critical values do quite well because of the underlying
856 multivariate normal dependence structure of the data. To study the robustness to the type
857 of association at extreme levels, 3000 new samples were generated from our non-
858 stationary GEV model but now with a dependence structure of a limiting extreme-value
859 distribution. This was achieved by generating the standard Gumbel residuals from an
860 equicorrelated multivariate Gumbel distribution as described by *Stephenson* [2003]. The
861 results (not shown) are very similar to those presented in Table C1 for a multivariate
862 normal dependence structure from which it may be concluded that the "MVN" critical
863 values are robust to the dependence structure.
864

865 **Acknowledgments.** We acknowledge the ENSEMBLES project, funded by the European
866 Commission's 6th Framework Programme through contract GOCE-CT-2003-505539.
867 The Alpine data set was kindly provided by MeteoSwiss.

868 **References**

869 Adlouni, S. El., T. B. M. J. Ouarda, X. Zhang, R. Roy, and B. Bobée (2007), Generalized
870 maximum likelihood estimators for the nonstationary generalized extreme value model,
871 *Water Resour. Res.*, *43*, W03410, doi:10.1029/2005WR004545.

872 Alila, Y. (1999), A hierarchical approach for the regionalization of precipitation annual
873 maxima in Canada, *J. Geophys. Res.*, *104*(D24), 31,645–31,655.

874 Anderson, T. W., and D. A. Darling (1952), Asymptotic theory of certain "goodness of
875 fit" criteria based on stochastic processes, *Ann. Math. Stat.*, *23*(2), 193–212,
876 doi:10.1214/aoms/1177729437.

877 Arnell, N. W., and S. Gabriele (1988), The performance of the two-component extreme
878 value distribution in regional frequency analysis, *Water Resour. Res.*, *24*(6), 879–887.

879 Beniston, M., D. B. Stephenson, O. B. Christensen, C. A. T. Ferro, C. Frei, S. Goyette, K.
880 Halsnaes, T. Holt, K. Jylhä, B. Koffi, J. Palutikof, R. Schöll, T. Semmler, and K. Woth
881 (2007), Future extreme events in European climate: an exploration of regional climate
882 model projections, *Climatic Change*, *81*, 71–95, doi:10.1007/s10584-006-9226-z.

883 Brath A., A. Castellarin, and A. Montanari (2003), Assessing the reliability of regional
884 depth-duration-frequency equations for gaged and ungaged sites, *Water Resour. Res.*,
885 *39*(12), 1367, doi:10.1029/2003WR002399.

886 Brohan, P., J. J. Kennedy, I. Harris, S. F. B. Tett, and P. D. Jones (2006), Uncertainty
887 estimates in regional and global observed temperature changes: A new data set from
888 1850, *J. Geophys. Res.*, *111*, D12106, doi:10.1029/2005JD006548.

889 Brown, S. J., J. Caesar, and C. A. T. Ferro (2008), Global changes in extreme daily
890 temperature since 1950, *J. Geophys. Res.*, *113*, D05115, doi:10.1029/2006JD008091.

891 Buishand, T. A. (1991), Extreme rainfall estimation by combining data from several sites,
892 *Hydrological Sciences Journal*, *36*(4), 345–365.

893 Buonomo, E., R. Jones, C. Huntingford, and J. Hannaford (2007), On the robustness of
894 changes in extreme precipitation over Europe from two high resolution climate change
895 simulations, *Q. J. R. Meteorol. Soc.*, *133*, 65–81, doi:10.1002/qj.13.

896 Christensen, O. B., and J. H. Christensen (2004), Intensification of extreme European
897 summer precipitation in a warmer climate, *Global Planet. Change*, *44*, 107–117,
898 doi:10.1016/j.gloplacha.2004.06.013.

899 Cleveland, W. S. (1979), Robust locally weighted regression and smoothing scatterplots,
900 *J. Am. Stat. Assoc.*, *74*, 829–836.

901 Coelho, C. A., C. A. T. Ferro, D. B. Stephenson, and D. J. Steinskog (2008), Methods for
902 exploring spatial and temporal variability of extreme events in climate data, *J. Clim.*,
903 *21*(10), 2072–2092, doi:10.1175/2007JCLI1781.1.

904 Coles, S. (2001), *An Introduction to Statistical Modeling of Extreme Values*, Springer-
905 Verlag, New York.

906 Cunderlik, J. M., and D. H. Burn (2003), Non-stationary pooled flood frequency analysis,
907 *J. Hydrol.*, *276*, 210–223.

908 Cunderlik, J. M., and T. B. M. J. Ouarda (2006), Regional flood-duration-frequency
909 modeling in the changing environment, *J. Hydrol.*, *318*, 276–291.

910 Davison, A. C., and D. V. Hinkley (1997), *Bootstrap methods and their application*,
911 Cambridge University Press.

912 Durman, C. F., J. M. Gregory, D. C. Hassell, R. G. Jones, and J. M. Murphy (2001), A
913 comparison of extreme European daily precipitation simulated by a global and regional
914 climate model for present and future climates, *Q. J. R. Meteorol. Soc.*, *127*, 1005–1015.

915 Ekström, M., H. J. Fowler, C. G. Kilsby, and P. D. Jones (2005), New estimates of future
916 changes in extreme rainfall across the UK using regional climate model integrations. 2.
917 Future estimates and use in impact studies, *J. Hydrol.*, *300*, 234–251,
918 doi:10.1016/j.jhydrol.2004.06.019.

919 Faulkner, D. S., and D. A. Jones (1999), The FORGEX method of rainfall growth
920 estimation III: Examples and confidence intervals. *Hydrol. Earth Syst. Sci.*, *3*, 205–212.

921 Fowler, H. J., M. Ekström, C. G. Kilsby, and P. D. Jones (2005), New estimates of future
922 changes in extreme rainfall across the UK using regional climate model integrations, 1.
923 Assessment of control climate, *J. Hydrol.*, *300*, 212–233,
924 doi:10.1016/j.jhydrol.2004.06.017.

925 Frei, C., and C. Schär (1998), A precipitation climatology of the Alps from high-
926 resolution rain-gauge observations, *Int. J. Climatol.*, *18*(8), 873–900.

927 Frei, C., and C. Schär (2001), Detection probability of trends in rare events: Theory and
928 application to heavy precipitation in the Alpine region, *J. Clim.*, *14*, 1568–1584.

929 Frei, C., J. H. Christensen, M. Déqué, D. Jacob, R. G. Jones, and P. L. Vidale (2003),
930 Daily precipitation statistics in regional climate models: Evaluation and intercomparison
931 for the European Alps, *J. Geophys. Res.*, *108*(D3), 4124, doi:10.1029/2002JD002287.

932 Frei, C., R. Schöll, S. Fukutome, J. Schmidli, and P. L. Vidale (2006), Future change of
933 precipitation extremes in Europe: Intercomparison of scenarios from regional climate
934 models, *J. Geophys. Res.*, *111*, D06105, doi:10.1029/2005JD005965.

935 García, J. A., M. C. Gallego, A. Serrano, and J. M. Vaquero (2007), Trends in block-
936 seasonal extreme rainfall over the Iberian Peninsula in the second half of the twentieth
937 century, *J. Clim.*, *20*, 113–130, doi:10.1175/JCLI3995.1.

938 Giorgi, F., J. W. Hurrell, M. R. Marinucci, and M. Beniston (1997), Elevation
939 dependency of the surface climate change signal: A model study, *J. Clim.*, *10*, 288–296,
940 doi:10.1175/1520-0442(1997)010.

941 Goubanova, K., and L. Li (2007), Extremes in temperature and precipitation around the
942 Mediterranean basin in an ensemble of future climate scenario simulations, *Global*
943 *Planet. Change*, *57*, 27–42, doi:10.1016/j.gloplacha.2004.06.010.

944 Haylock, M. R., N. Hofstra, A. M. G. Klein Tank, E. J. Klok, P. D. Jones, and M. New
945 (2008), A European daily high-resolution gridded dataset of surface temperature and
946 precipitation, *J. Geophys. Res.*, *113*, D20119, doi:10.1029/2008JD010201.

947 Heffernan, J. E., and J. A. Tawn (2004), A conditional approach for multivariate extreme
948 values (with discussion), *J. R. Stat. Soc. B*, *66*(3), 497–546, doi:10.1111/j.1467-
949 9868.2004.02050.x.

950 Hofstra, N., M. Haylock, M. New, and P. D. Jones (2009), Testing E-OBS European
951 high-resolution gridded dataset of daily precipitation and surface temperature, *J.*
952 *Geophys. Res.*, submitted.

953 Hosking, J. R. M., and J. R. Wallis (1997), *Regional frequency analysis*, Cambridge
954 University Press.

955 Hundecha, Y., and A. Bárdossy (2005), Trends in daily precipitation and temperature
956 extremes across western Germany in the second half of the 20th century, *Int. J. Climatol.*,
957 *25*, 1189–1202, doi:10.1002/joc.1182.

958 Huntingford, C., R. G. Jones, C. Prudhomme, R. Lamb, J. H. C. Gash, and D. A. Jones
959 (2003), Regional climate model predictions of extreme rainfall for a changing climate, *Q.*
960 *J. R. Meteorol. Soc.*, *129*, 1607–1621, doi:10.1256/qj.02.97.

961 Jungclaus, J. H., N. Keenlyside, M. Botzet, H. Haak, J.-J. Luo, M. Latif, J. Marotzke, U.
962 Mikolajewitcz, and E. Roeckner (2006), Ocean circulation and tropical variability in the
963 coupled model ECHAM5/MPI-OM, *J. Clim.*, *19*, 3952–3972, doi:10.1175/JCLI3827.1.

964 Kendon, E. J., R. G. Jones, and E. Buonomo (2008), Robustness of future changes in
965 local precipitation extremes, *J. Clim.*, *21*, 4280–4297, doi:10.1175/2008JCLI2082.1.

966 Kharin, V. V., and F. W. Zwiers (2005), Estimating extremes in transient climate change
967 simulations, *J. Clim.*, *18*, 1156–1173, doi:10.1175/JCLI3320.1.

968 Kharin, V. V., F. W. Zwiers, X. Zhang, and G. C. Hegerl (2007), Changes in temperature
969 and precipitation extremes in the IPCC ensemble of global coupled model simulations, *J.*
970 *Clim.*, *20*, 1419–1444, doi:10.1175/JCLI4066.1.

971 Kyselý, J., and J. Picek (2007), Regional growth curves and improved design value
972 estimates of extreme precipitation events in the Czech Republic, *Clim. Res.*, *33*, 243–255.

973 Laio, F. (2004), Cramer-von Mises and Anderson-Darling goodness of fit tests for
974 extreme value distributions with unknown parameters, *Water Resour. Res.*, *40*, W09308,
975 doi:10.1029/2004WR003204.

976 Leander, R., T. A. Buishand, B. J. J. M. van den Hurk, and M. J. M. de Wit (2008),
977 Estimated changes in flood quantiles of the river Meuse from resampling of regional
978 climate model output, *J. Hydrol.*, *351*, 331–343, doi:10.1016/j.jhydrol.2007.12.020.

979 Lettenmaier, D. P., J. R. Wallis, and E. Wood (1987), Effect of regional heterogeneity on
980 flood frequency estimation, *Water Resour. Res.*, *23*(2), 313–323.

981 van Meijgaard, E., L. H. van Ulft, W. J. van de Berg, F. C. Bosveld, B. J. J. M. van den
982 Hurk, G. Lenderink, and A. P. Siebesma (2008), The KNMI regional atmospheric climate
983 model RACMO, version 2.1, *KNMI Technical Report 302*, Royal Netherlands
984 Meteorological Institute, De Bilt, Netherlands.

985 Nakićenović, N., and R. Swart (Eds.) (2000), *Special Report on Emissions Scenarios. A*
986 *Special Report of Working Group III of the Intergovernmental Panel on Climate Change*,
987 Cambridge University Press.

988 Northrop, P. J. (2004), Likelihood-based approaches to flood frequency estimation, *J.*
989 *Hydrol.*, *292*, 96–113, doi:10.1016/j.jhydrol.2003.12.031.

990 Pall, P., M. R. Allen, and D. A. Stone (2007), Testing the Clausius-Clapeyron constraint
991 on changes in extreme precipitation under $CO_2$ warming, *Clim. Dyn.*, *28*, 351–363,
992 doi:10.1007/s00382-006-0180-2.

993 Renard, B., V. Garreta, and M. Lang (2006), An application of Bayesian analysis and
994 Markov chain Monte Carlo methods to the estimation of a regional trend in annual
995 maxima, *Water Resour. Res.*, *42*, W12422, doi:10.1029/2005WR004591.

996 Schaefer, M. G. (1990), Regional analyses of precipitation annual maxima in Washington
997 State, *Water Resour. Res.*, *26*(1), 119–131.

998 Sen, P. K. (1968), Estimation of the regression coefficient based on Kendall's tau, *J. Am.*
999 *Stat. Assoc.*, *63*, 1379–1389.

1000 Shimokawa, T., and M. Liao (1999), Goodness of fit tests for type-1 extreme-value and
1001 2-parameter Weibull distributions, *IEEE Trans. Reliab.*, *48*(1), 79–86.

1002 Stephenson, A. (2003), Simulating multivariate extreme value distributions of logistic
1003 type, *Extremes*, *6*, 49–59.

1004 Sveinsson, O. G. B., D. C. Boes, and J. D. Salas (2001), Population index flood method
1005 for regional frequency analysis, *Water Resour. Res.*, *37*(11), 2733–2748.

1006 Zwiers, F. W., and V. Kharin (1998), Changes in the extremes of the climate simulated
1007 by CCC GCM2 under $CO_2$ doubling, *J. Clim.*, *11*(9), 2200–2222, doi: 10.1175/1520-
1008 0442(1998)011.

## List of Figures

**Figure 1.** (a) The river Rhine basin. (b) The dispersion coefficient of the 1-day summer (JJA) maxima for the fit of the stationary GEV model to the RACMO-ECHAM5 simulation for the period 1950–1989. (c) Same as (b) but for the period 2070–2099. (d) Subdivision of the river Rhine basin into five regions. The numbers in subscript give the number of grid boxes included in the region. The rectangles represent the RACMO model grid boxes, the gray dots show the locations of stations that have been used for gridding of the E-OBS data.

**Figure 2.** Relative change of mean seasonal and annual precipitation between the periods 1950–1989 and 2070–2099 in the RACMO-ECHAM5 simulation for all 5 regions of the Rhine basin.

**Figure 3.** Summer (JJA) and winter (DJF) global temperature anomalies in the ECHAM5 simulation.

**Figure 4.** (a–c) Estimates of the GEV parameters for the 1-day summer (JJA) precipitation extremes for the period 1950–1989 for the ALP, E-OBS, and RACMO-ECHAM5 data. The results are averaged over the region in the case of the location parameter. (d–f) The changes of the GEV parameters for the 1-day summer (JJA) precipitation extremes between the periods 1950–1989 and 2070–2099. The boxplots were obtained from 3000 bootstrap samples. The boxes represent the interquartile range, the whiskers extend from the 5th to the 95th percentile of these bootstrap samples.

**Figure 5.** Relative changes of quantiles of the 1-day summer maximum precipitation between the periods 1950–1989 and 2070–2099 in the RACMO-ECHAM5 simulation for all five regions. The confidence bands were obtained from 3000 bootstrap samples. The 5th, 25th, 50th, 75th, and 95th percentile of these bootstrap samples are shown.

**Figure 6.** Same as Figure 5 but for the restricted model with common trends over regions 1, 3, 4, and 5. The panel on the right gives the average relative change of the four regions together with the average confidence band.

**Figure 7.** The values of the Anderson-Darling statistic for (a) region 1 and (b) region 3 for the 1-day summer (JJA) precipitation extremes in the RACMO-ECHAM5 simulation.

**Figure 8.** Summary of the goodness of fit testing of the non-stationary GEV model for the 1-day summer (JJA) precipitation extremes in the RACMO-ECHAM5 simulation.

**Figure 9.** Averaged standard normal residuals (gray line) for the 1-day summer (JJA) precipitation extremes in the RACMO-ECHAM5 simulation in region 1. The black line shows residuals smoothed by locally weighted regression "loess".

**Figure 10.** Average autocorrelation coefficients (ACC) of the standard normal residuals (vertical bars) for the 1-day summer (JJA) precipitation extremes in the RACMO-

ECHAM5 simulation in region 1. The 90% confidence band (shaded area) was obtained from 3000 bootstrap samples.

**Figure 11.** Same as Figure 4 but for the 5-day winter (DJF) precipitation extremes.

**Figure 12.** Same as Figure 5 but for the 5-day winter (DJF) precipitation extremes.

**Figure 13.** Same as Figure 8 but for the 5-day winter (DJF) precipitation extremes.

**Figure 14.** Grid box estimates of the trend in the location parameter as a function of altitude for the 5-day winter (DJF) precipitation maxima in the RACMO-ECHAM5 simulation. The values for the grid boxes in region 1 (black dots) are smoothed by locally weighted regression "loess" (black line).

**Table 1.** Reduction (%) of interquartile ranges of the parameter estimates due to spatial pooling for the summer (JJA) in the case of the RACMO-ECHAM5 data.

| | region | | | | | |
|---|---|---|---|---|---|---|
| parameter | 1 | 2 | 3 | 4 | 5 | mean |
| $\xi_1$ | 37 | 32 | 34 | 31 | 39 | 35 |
| $\gamma_0$ | 58 | 45 | 48 | 53 | 44 | 50 |
| $\gamma_1$ | 67 | 60 | 60 | 61 | 58 | 61 |
| $\kappa_0$ | 73 | 71 | 67 | 66 | 58 | 67 |
| $\kappa_1$ | 80 | 75 | 75 | 72 | 66 | 74 |

**Table 2.** The *p*-values resulting from the test for differences between regions for the summer (JJA).

| parameter | *p*-value |
|---|---|
| $\xi_1$ | 0.01 |
| $\gamma_0$ | 0.00 |
| $\gamma_1$ | 0.13 |
| $\kappa_0$ | 0.00 |
| $\kappa_1$ | 0.00 |

1074 **Table 3.** Sensitivity of the changes in the GEV parameters and the 2-, 10-, and 50-year
1075 quantiles to the choice of the time indicator $I(t)$. Changes are the absolute (shape
1076 parameter) or relative changes (other GEV parameters and quantiles) in these parameters
1077 and quantiles between the periods 1950–1989 and 2070–2099. The results are averaged
1078 over regions 1, 3, 4, and 5.

| temperature anomaly used as $I(t)$ | | $\xi$ | $\gamma$ | $\kappa$ | $Q_2$ | $Q_{10}$ | $Q_{50}$ |
|---|---|---|---|---|---|---|---|
| summer | global | 1.03 | 1.26 | 0.067 | 1.06 | 1.20 | 1.33 |
| | global smoothed | 1.01 | 1.25 | 0.067 | 1.04 | 1.17 | 1.30 |
| | RACMO domain smoothed | 1.02 | 1.24 | 0.060 | 1.05 | 1.17 | 1.29 |
| | Rhine basin smoothed | 1.01 | 1.26 | 0.073 | 1.03 | 1.17 | 1.30 |
| annual | global | 1.03 | 1.26 | 0.069 | 1.06 | 1.20 | 1.33 |
| | global smoothed | 1.01 | 1.25 | 0.066 | 1.04 | 1.17 | 1.30 |
| | RACMO domain smoothed | 1.02 | 1.24 | 0.059 | 1.05 | 1.17 | 1.29 |
| | Rhine basin smoothed | 1.01 | 1.25 | 0.065 | 1.04 | 1.17 | 1.29 |

1079

1080

**Table C1.** Local rejection rates and critical values (nominal significance level of 0.1) for testing goodness of fit using the Anderson-Darling statistic. The "true" critical values are based on 3000 simulated samples from a non-stationary GEV model, the critical values "HT" and "MVN" are based on 3000 bootstrap samples from one of these simulations using respectively the Heffernan and Tawn approach and a multivariate normal distribution to preserve spatial dependence.

| | rejection rate | | critical value | | |
|---|---|---|---|---|---|
| correlation | "HT" | "MVN" | "HT" | "MVN" | "true" |
| 0.00 | 0.098 | 0.102 | 0.881 | 0.870 | 0.875 |
| 0.40 | 0.077 | 0.095 | 0.888 | 0.837 | 0.823 |
| 0.60 | 0.050 | 0.088 | 0.901 | 0.778 | 0.751 |
| 0.80 | 0.025 | 0.081 | 0.892 | 0.686 | 0.648 |
| 0.99 | 0.000 | 0.093 | 0.905 | 0.523 | 0.514 |

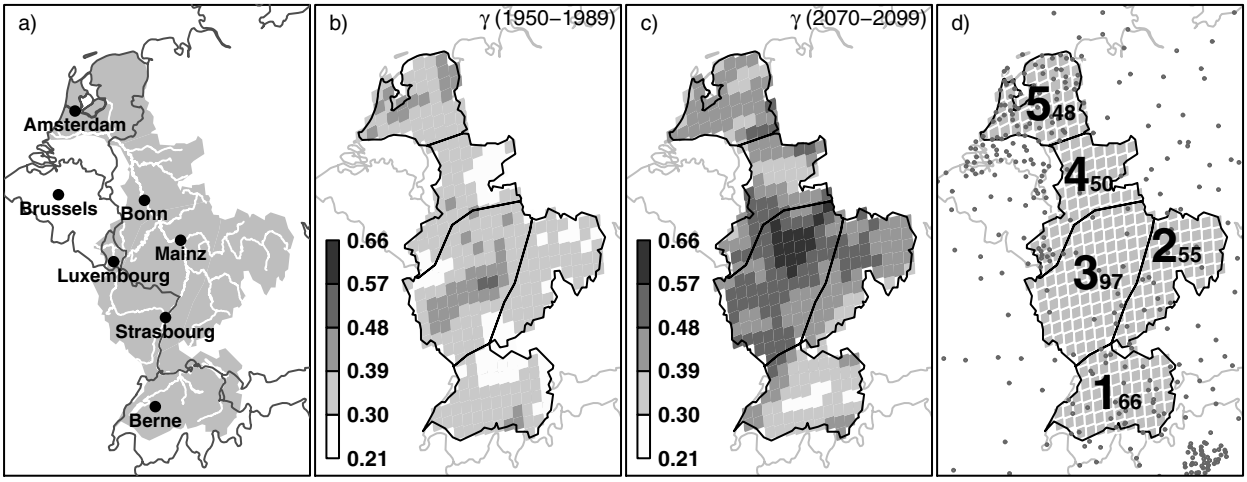


1088

1089 **Figure 1.** (a) The river Rhine basin. (b) The dispersion coefficient of the 1-day summer

1090 (JJA) maxima for the fit of the stationary GEV model to the RACMO-ECHAM5

1091 simulation for the period 1950–1989. (c) Same as (b) but for the period 2070–2099. (d)

1092 Subdivision of the river Rhine basin into five regions. The numbers in subscript give the

1093 number of grid boxes included in the region. The rectangles represent the RACMO model

1094 grid boxes, the gray dots show the locations of stations that have been used for gridding

1095 of the E-OBS data.

1096

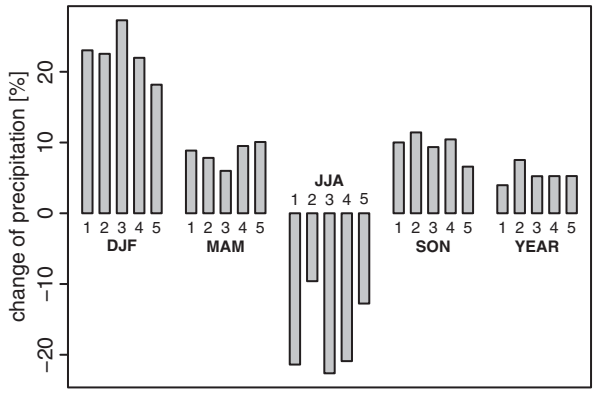


1097

1098 **Figure 2.** Relative change of mean seasonal and annual precipitation between the periods

1099 1950–1989 and 2070–2099 in the RACMO-ECHAM5 simulation for all 5 regions of the

1100 Rhine basin.

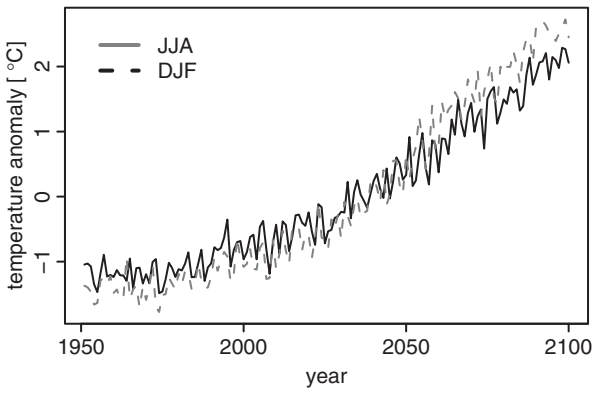


**Figure 3.** Summer (JJA) and winter (DJF) global temperature anomalies in the ECHAM5 simulation.

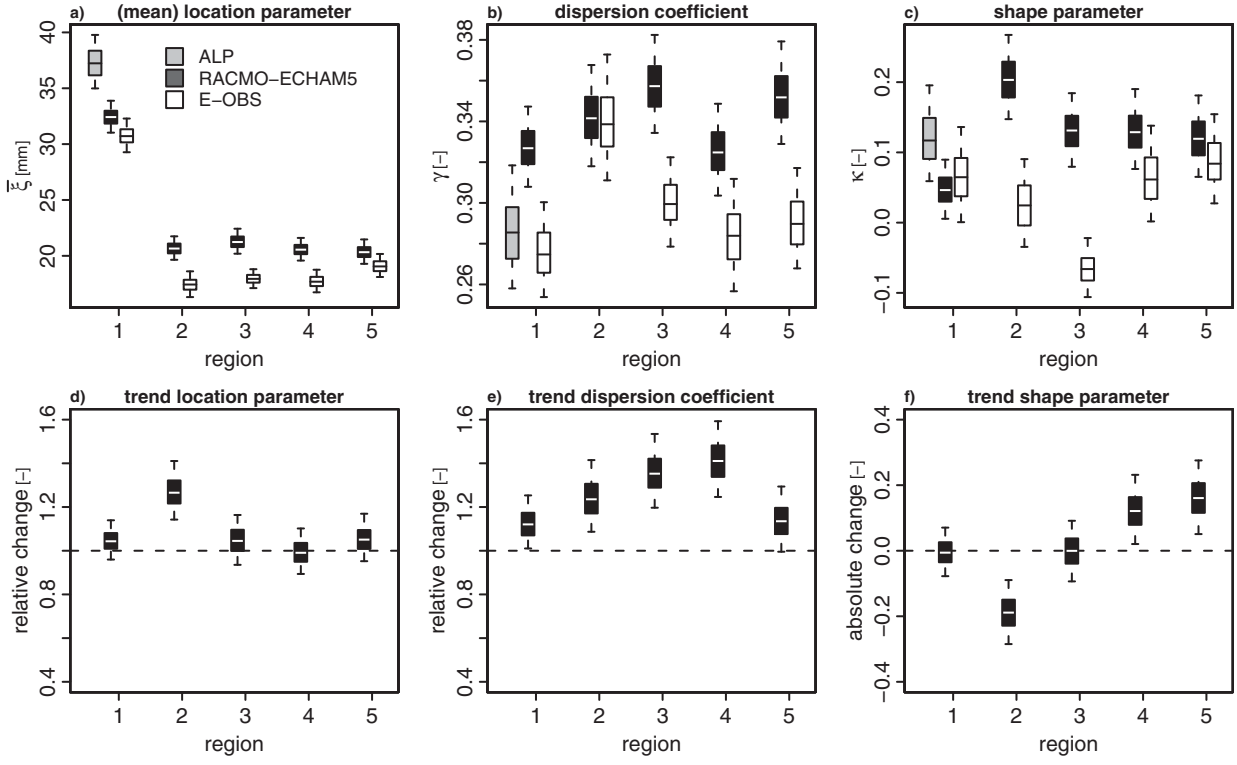


**Figure 4.** (a–c) Estimates of the GEV parameters for the 1-day summer (JJA) precipitation extremes for the period 1950–1989 for the ALP, E-OBS, and RACMO-ECHAM5 data. The results are averaged over the region in the case of the location

parameter. (d–f) The changes of the GEV parameters for the 1-day summer (JJA) precipitation extremes between the periods 1950–1989 and 2070–2099. The boxplots were obtained from 3000 bootstrap samples. The boxes represent the interquartile range, the whiskers extend from the 5th to the 95th percentile of these bootstrap samples.

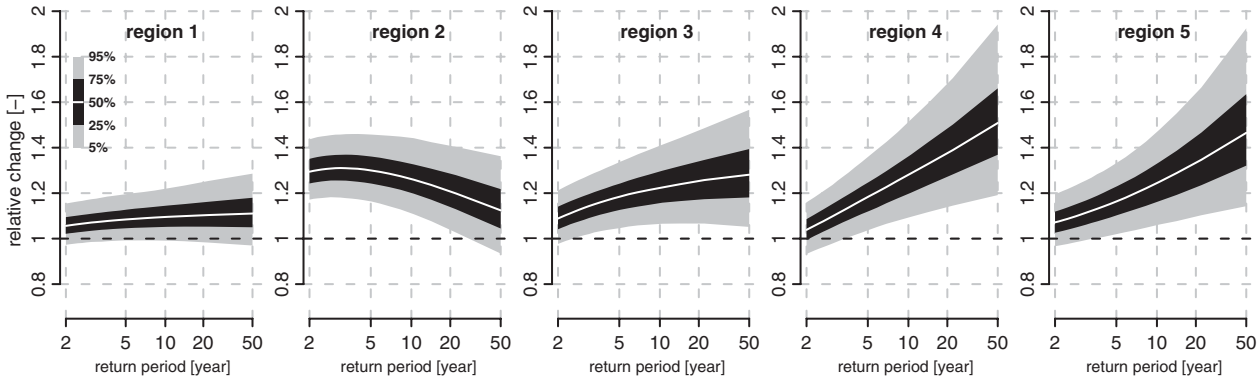


**Figure 5.** Relative changes of quantiles of the 1-day summer maximum precipitation between the periods 1950–1989 and 2070–2099 in the RACMO-ECHAM5 simulation for all five regions. The confidence bands were obtained from 3000 bootstrap samples. The 5th, 25th, 50th, 75th, and 95th percentile of these bootstrap samples are shown.

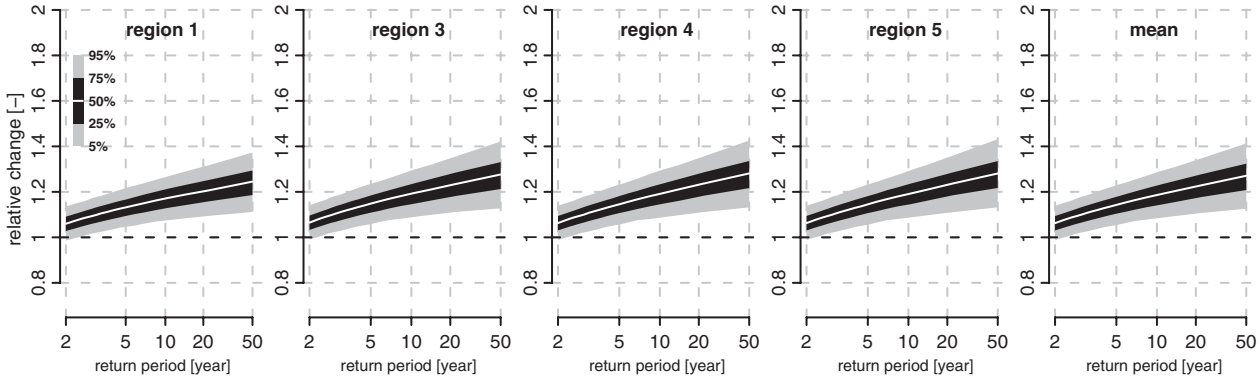

**Figure 6.** Same as Figure 5 but for the restricted model with common trends over regions 1, 3, 4 and 5. The panel on the right gives the average relative change of the four regions together with the average confidence band.

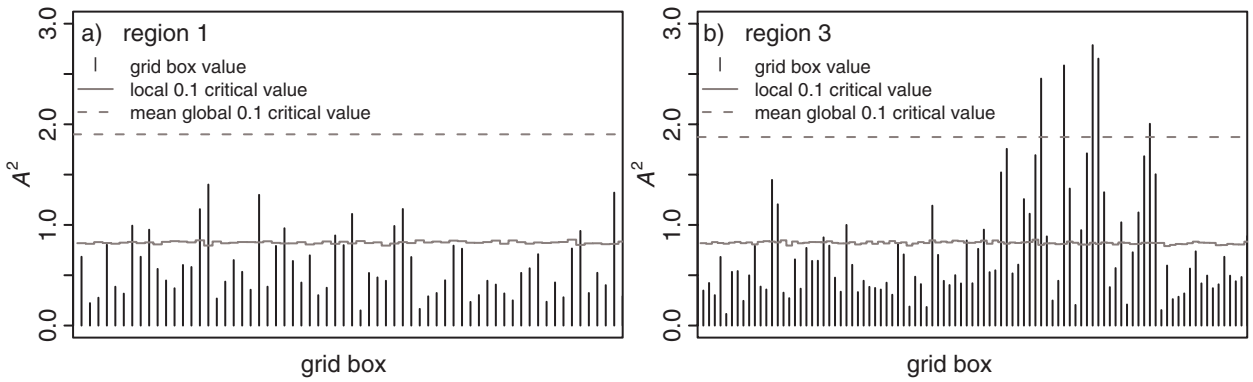


**Figure 7.** The values of the Anderson-Darling statistic for (a) region 1 and (b) region 3 for the 1-day summer (JJA) precipitation extremes in the RACMO-ECHAM5 simulation.


**Figure 8.** Summary of the goodness of fit testing of the non-stationary GEV model for the 1-day summer (JJA) precipitation extremes in the RACMO-ECHAM5 simulation.

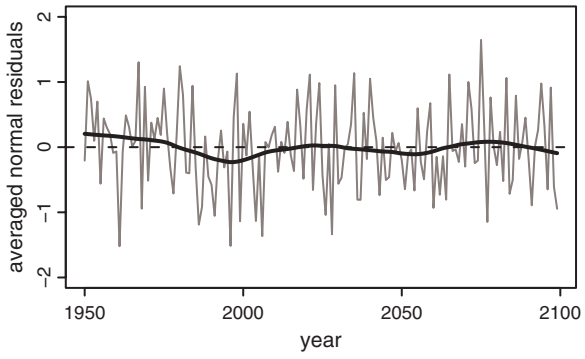


**Figure 9.** Averaged standard normal residuals (gray line) for the 1-day summer (JJA) precipitation extremes in the RACMO-ECHAM5 simulation in region 1. The black line shows residuals smoothed by locally weighted regression "loess".

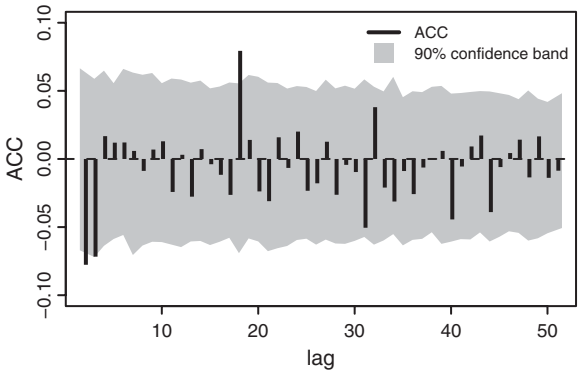


**Figure 10.** Average autocorrelation coefficients (ACC) of the standard normal residuals (vertical bars) for the 1-day summer (JJA) precipitation extremes in the RACMO-ECHAM5 simulation in region 1. The 90% confidence band (shaded area) was obtained from 3000 bootstrap samples.

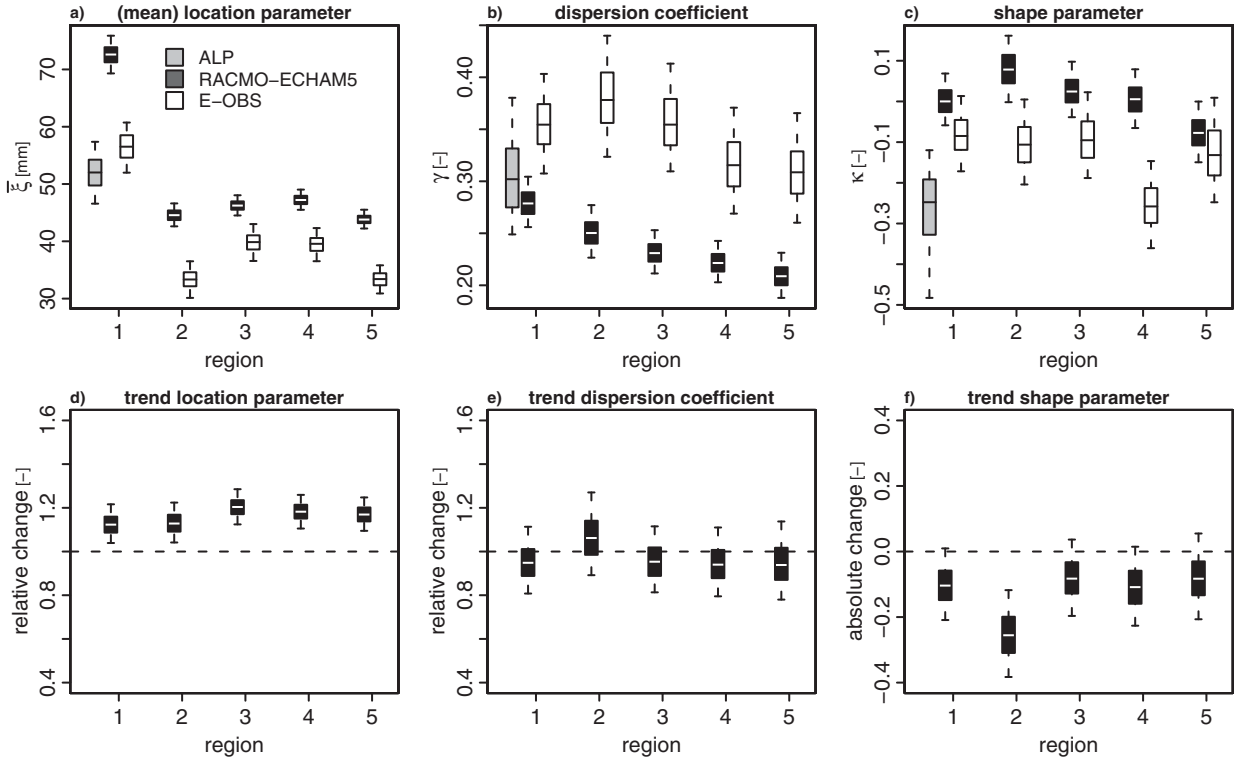


1145

1146 **Figure 11.** Same as Figure 4 but for the 5-day winter (DJF) precipitation extremes.

1147

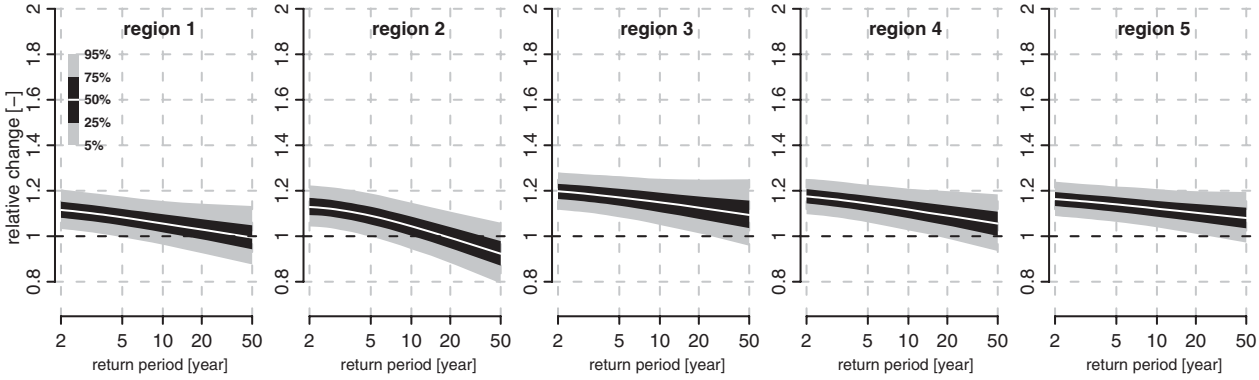


1148

1149 **Figure 12.** Same as Figure 5 but for the 5-day winter (DJF) precipitation extremes.

1150


1151

1152 **Figure 13.** Same as Figure 8 but for the 5-day winter (DJF) precipitation extremes.

1153

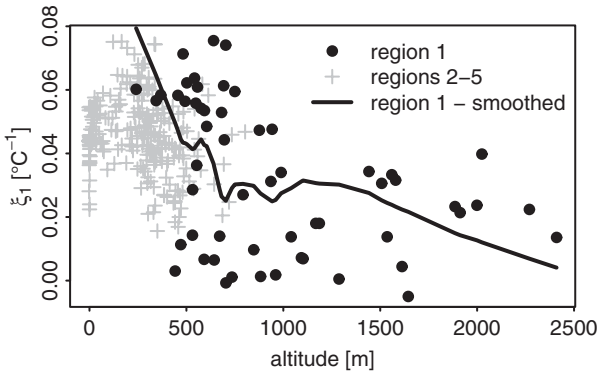


1154

1155 **Figure 14.** Grid box estimates of the trend in the location parameter as a function of

1156 altitude for the 5-day winter (DJF) precipitation maxima in the RACMO-ECHAM5

1157 simulation. The values for the grid boxes in region 1 (black dots) are smoothed by locally

1158 weighted regression "loess" (black line).